Electronic Supplementary Material (ESI) for Journal of Materials Chemistry C.

Supplementary Information for

Revealing the correlation relation between conducting channels in self-assembled monolayer tunnel junctions

Shu Zhu[1], Xiang Li[1], Wenrui Xu[1], Qianqian Guo[1], Wei Du[1,*], Tao Wang[1,*]

[1]Institute of Functional Nano & Soft Materials (FUNSOM), Jiangsu Key Laboratory for Carbon-Based Functional Materials & Devices, Soochow University, 199 Ren'ai Road, Suzhou, 215123, Jiangsu, P. R. China

[*]E-mail: wangtao2019@suda.edu.cn; duwei2021@suda.edu.cn

S1. Experimental details.

Preparation of micropore-confined SAM tunnel junctions: The micropore-confined SAM tunnel junctions were prepared as followed (Fig. S1). First, a 30 nm Au film was deposited via electron beam evaporation (Beijing Vnano Vacuum Technology. Co., Ltd.) on a clean p-type Si (111) wafer. After that, the optical adhesive (Norland, no. 61) was dropped on the substrate to paste cleaned 22×22 mm^2 coverslips. The coverslips were cured by 45 min exposure to ultraviolet light (100 W), and cleaved from the cured wafer to form the template stripped Au (Au^{TS}) bottom electrodes. Second, SiO_2 microspheres (Suzhou Knowledge & Benefit Sphere Tech. Co., Ltd.) with a diameter of 20 μm were dispersed on the Au^{TS} substrate. Then, 60 nm Al_2O_3 was deposited on the substrate by electron beam evaporation to form an insulating layer. After Al_2O_3 deposition, the microspheres were removed from the substrate by a stream of N_2 gas to obtain the micropore-confined Au^{TS} substrate. Third, the micropore-confined Au^{TS} substrate was cleaned for 30 min by the ultraviolet cleaner (Leno Science Co., Ltd.). Then, the Au^{TS} substrate was immersed in a degassed decanethiol solution (~3 mM, decanethiols from Sigma-Aldrich) for more than 3 h under the nitrogen atmosphere to form the decanethiolate SAM. For the 1,1′-biphenyl-4-thiol ($H-(C_6H_4)_2-SH$, BPT) SAM case (from Sigma-Aldrich), the micropore-confined Au^{TS} substrate was immersed into 1 mM solution under the nitrogen atmosphere for 24 h. Finally, a freshly formed EGaIn cone tip was used to contact with the SAM confined in the micropore structure, which is ready for the electrical or light emission measurements.

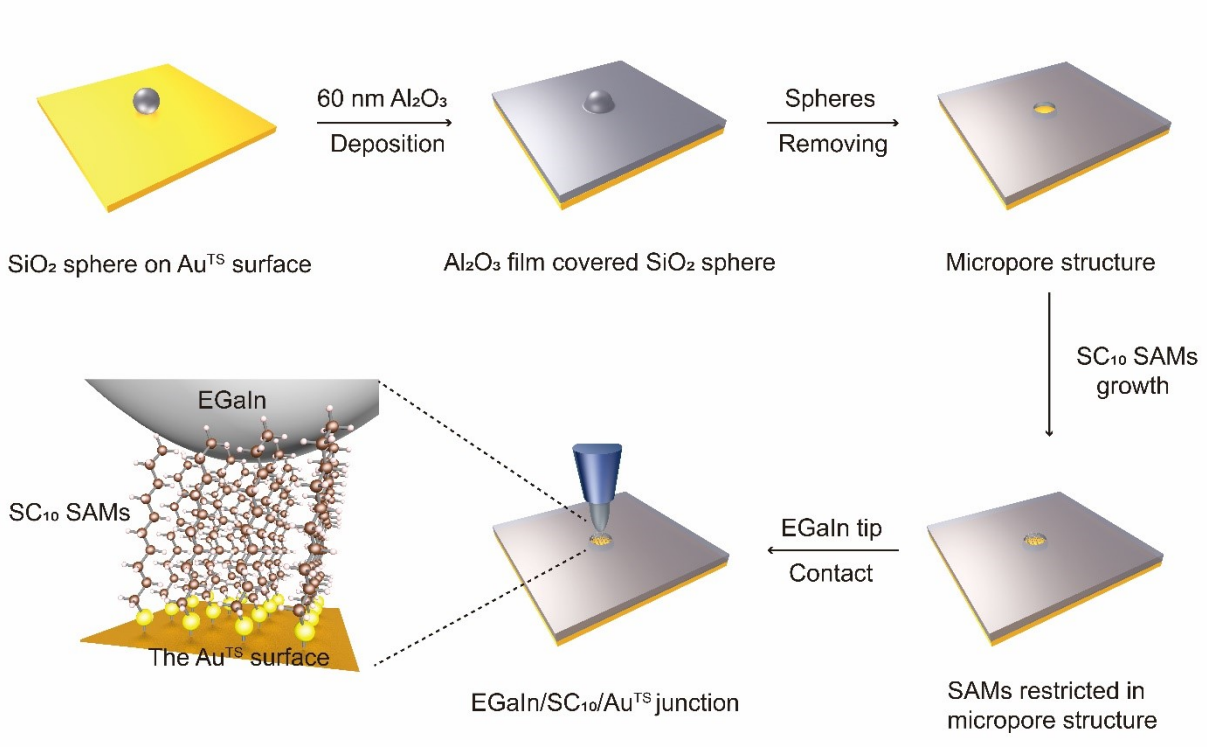

Figure S1. Schematic illustration of the fabrication procedure for the micropore device.

Surface characterization: The atomic force microscopy (AFM) and scanning electron microscopy (SEM) of the Au^{TS} surface and the micropore structure in Fig. 1b and Fig. S2 were conducted by the tapping-mode Veeco AFM (Bruker) and SEM (Zeiss G500), respectively.

Electrical measurements: For electrical measurements, the junctions were formed with a fresh EGaIn tip as the top electrode, and it was pressed down as much as possible to ensure full contact to SAM within the micropore. For each junction, 20 $J(V)$ traces were recorded in the bias range of $\pm$0.5 V (steps of 0.05 V) using a source meter (Keithley 4200 SCS). For each bias, we plotted the histogram of Log $|J|$ and fitted it with the Gaussian distribution to find the Gaussian mean value of Log $|J|$ and the Log standard deviation ($\sigma_{\log|J|}$). Then the Log $J(V)$ curves with error bars ($\sigma_{\log|J|}$) were plotted together with a colored heat map, where the color code describes the number of data points within the statistical area which corresponds to the

histogram of Log |*J*| for each bias, as shown in Fig. S5. Using a similar procedure, we also recorded the Log *J*(*V*) curves under high electrical biases, which is shown in Fig. S6. We note that, with the micropore, the yield of the molecular junction formation is almost 100%, which may be due to the lower imperfection of the top EGaIn contact to the SAMs with a smaller contact area.

Light emission measurements: During the measurements, a constant voltage was applied between the EGaIn tip and the Au^{TS} substrate via a source meter (Keithley 6430). The tunnelling induced light emission from the micropore-confined SAM tunnel junctions was captured through an inverted optical microscope (Nikon Eclipse Ti-E) equipped with a 100× oil objective (NA = 1.30) and an electron-multiplying charge coupled device (EMCCD, iXon Ultra 897). To following the light emission kinetics, light emission videos of 60 frames (2 second for each frame) were recorded with 300 EM gain. For spectral measurements, the Horiba spectrometer (IHR550) with a liquid-nitrogen-cooled CCD (Symphony) was used. In our experiments, the number of light emission spots is largely reduced with the micropore and ranges randomly from 2 to 6 at most cases.

Correlation analysis: A nonparametric Spearman rank correlation was used to analyse a monotonic correlation between every two sets of intensity time traces. For statistical analysis, the significance level of the *S* values was set to 0.05.

S2. AFM characterization.

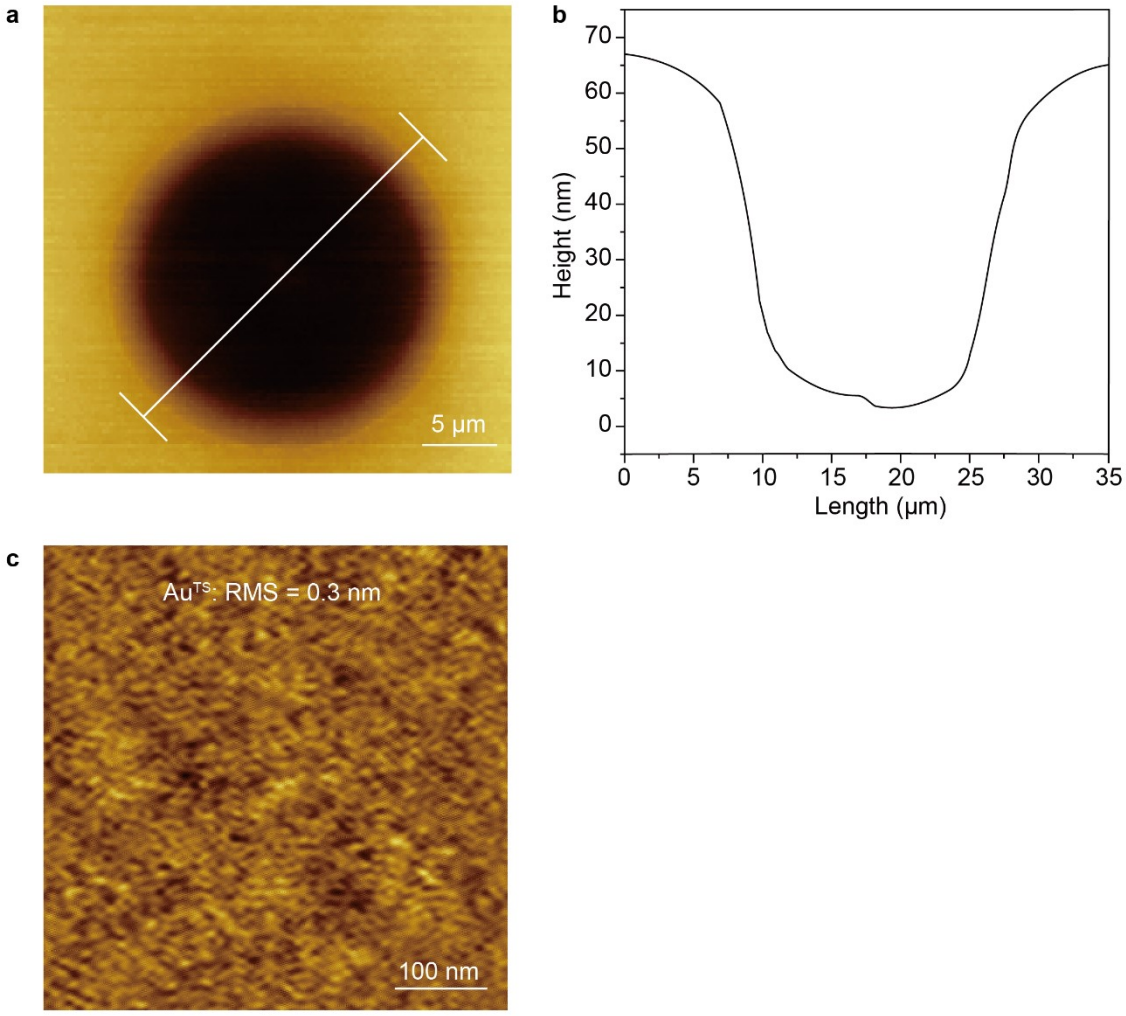

Figure S2. AFM characterization. **a)** AFM characterization of the Al_2O_3 micropore structure. **b**) The height profile of the Al_2O_3 micropore structure. **c**) AFM characterization of the Au^{TS} surface inside the micropore.

S3. Optical micrograph of the micropore-confined EGaIn junction.

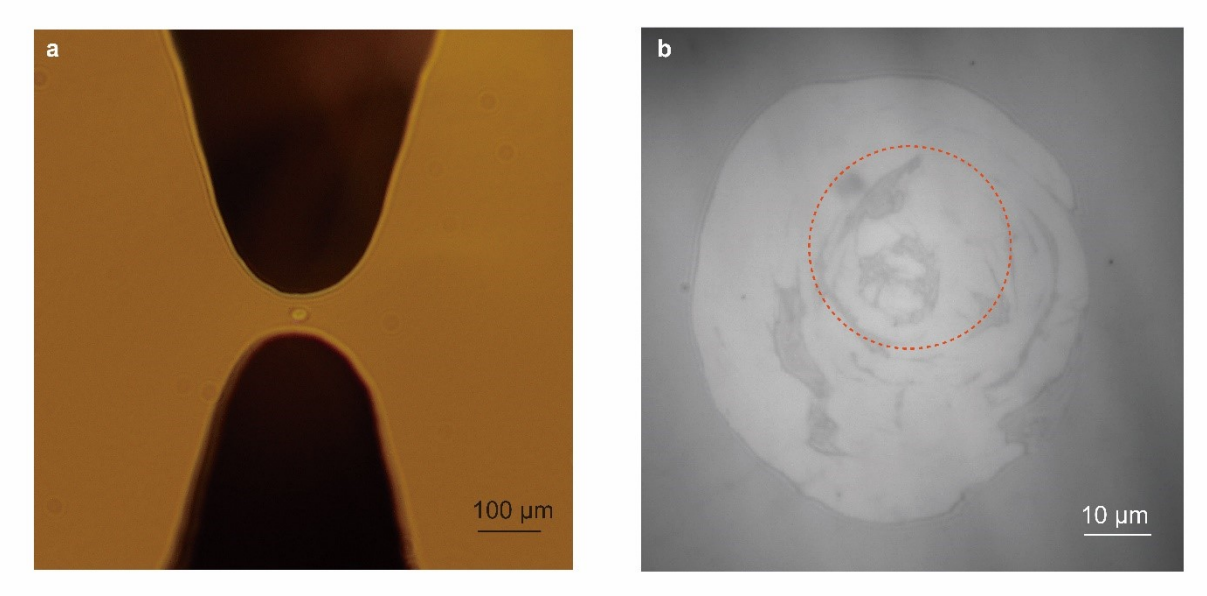

Figure S3. Optical micrograph of the micropore-confined EGaIn junction. **a**) The optical image of the micropore-confined EGaIn junction before the contact, where the micropore is clearly seen. The image was taken with a side camera. **b**) The optical image of the micropore with the EGaIn top electrode. The image was taken from the backside using an oil immersion objective and EMCCD camera. The red circle indicates the boundary of the Al_2O_3 micropore which limits the geometric contact area of the junction.

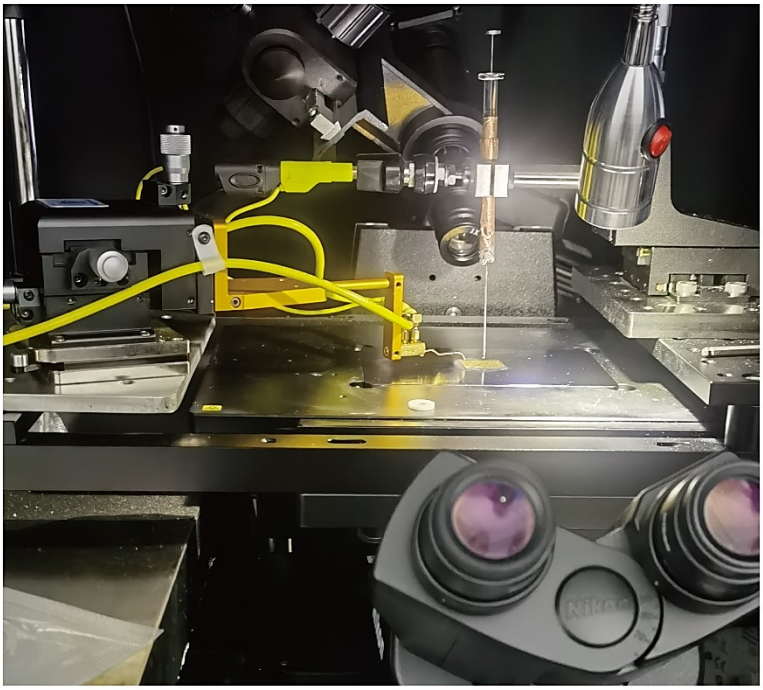

Figure S4. Photo of the EGaIn-based molecular monolayer tunnel junction on the inverted optical microscope.

S4. Electrical measurements of the alkanethiolate SAMs.

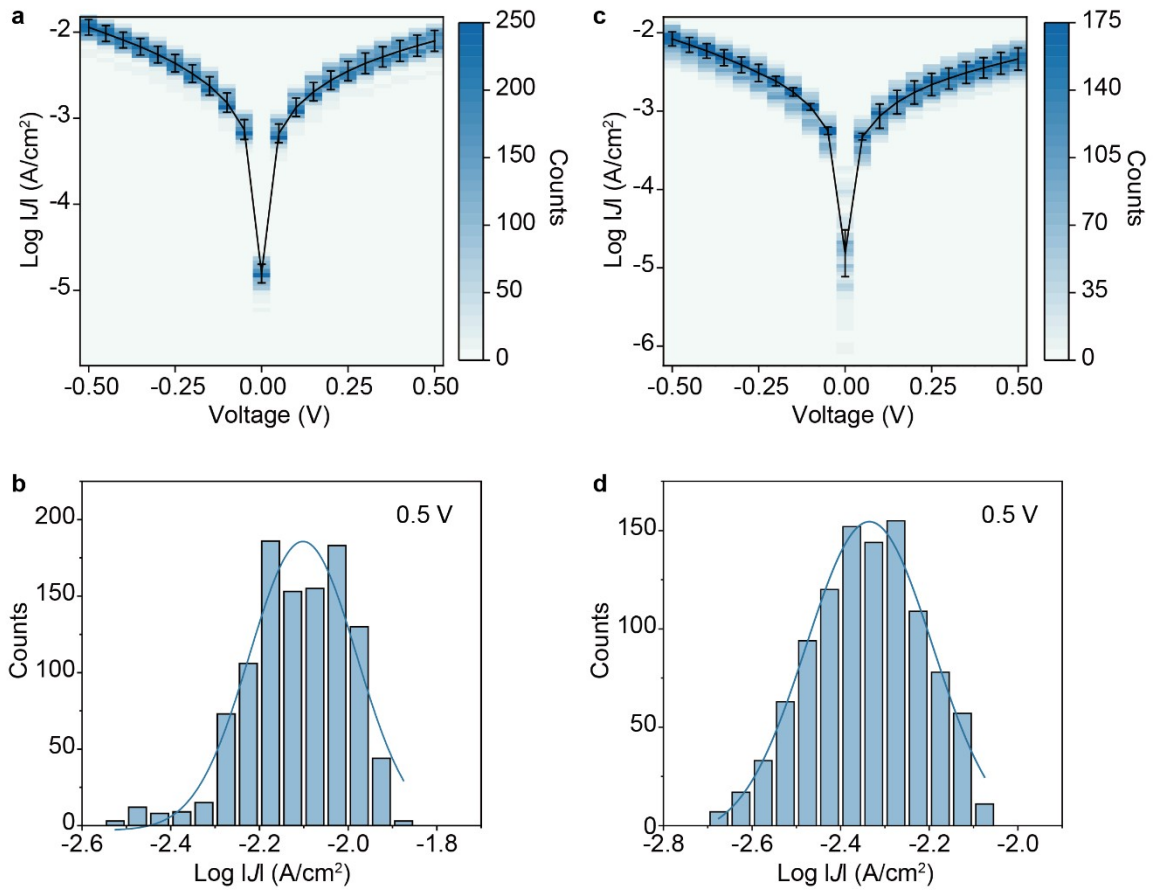

Figure S5. Electrical measurements of the Log $J(V)$ curves for junctions with SC_{10} SAMs. **a, b**) Log $J(V)$ plot for SC_{10} SAMs grown on the bare Au^{TS} substrates (a) and the histogram of Log $|J|$ measured at 0.5 V (b). **c,d)** Log $J(V)$ plot for SC_{10} SAMs grown on the micropore-confined structure (c) and the histogram of Log $|J|$ measured at 0.5 V (d). In panels (a) and (c), the color code describes the number of data points within the statistical area, which corresponds to the histogram of Log $|J|$ for each bias. The black lines depict the averaged Log $J(V)$ characteristics, and the error bars represent the standard deviations based on the Gaussian fit of the histogram at each bias. More than 20 junctions (26 junctions for SC_{10} restricted in micropores, and 27 junctions for SC_{10} on bare Au^{TS}) were measured. For each junction, 20 $J(V)$ traces were recorded in the bias range of ±0.5 V with a step of 0.05 V. In both cases, the

measured current densities are close to the previously reported values.[1-3]

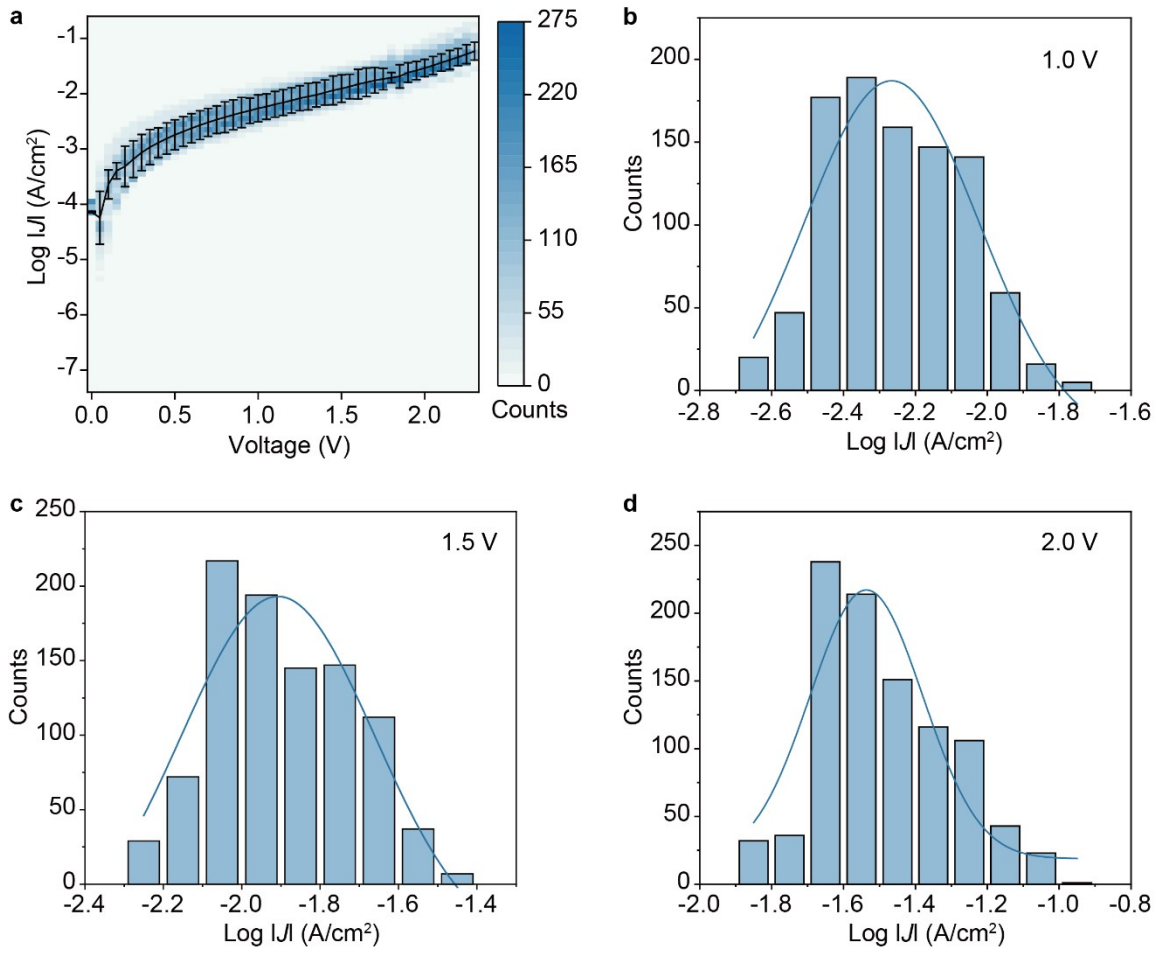

Figure S6. Electrical measurement of the Log $J(V)$ curve for junctions with SC_{10} SAMs in a larger bias range of 0 to 2.3 V. **a**) Log $J(V)$ plot for SC_{10} SAMs in the bias range of 0 to 2.3 V. **b,c,d**) Histograms of Log $|J|$ measured at 1.0 V (b), 1.5 V (c) and 2.0 V (d). 24 junctions were measured, while for each junction, 20 $J(V)$ traces were recorded with a step of 0.05 V.

S5. Estimation of the molecule number in each conducting channel.

We could estimate the number of molecules in each conducting channel with the following steps. First, the conductance of the whole junction can be estimated with the *J*(V) characteristics at low bias (<0.1 V). With a linear fitting (Figure S7), the conductance of the junction is found to be about 0.032 μS, which corresponds to 0.42×10^{-3} G_0. Then, compared to the measured conductance about 2×10^{-5} G_0 of a single decanethiol,[4] there are about 46 molecules involved in the whole monolayer junction by considering the parallel summation of the conductance from all molecules. Thus, for a junction with 2 or 6 emission spots (i.e. 2 or 6 conducting channels), each channel has about 21 or 7 molecules on average, respectively.

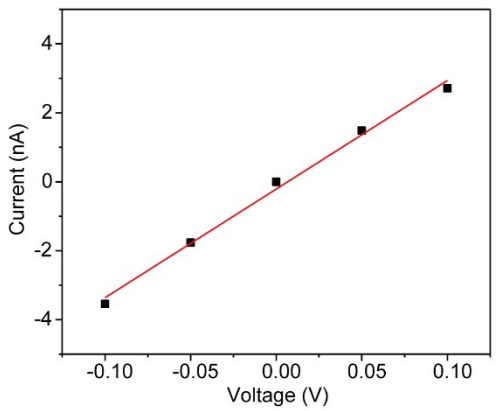

Figure S7. Linear fitting of *J*(V) in the bias range of ±0.1 V for conductance estimation. The *J*(V) data is from Figure S5c.

S6. Brief introduction about light emission in tunnel junctions.

Light emission (or plasmon emission) in tunnel junctions is mainly based on the inelastic tunnelling process where electrons tunnel through a thin (1–3 nm) tunnel barrier sandwiched between two metal electrodes inelastically. During inelastic tunnelling, tunnelling electrons have the chance to lose a portion of their energy to excite plasmons on the metallic electrode surface. Subsequently, these plasmons on the electrode surface can be out-coupled to far field as photon or light emission via scattering induced by surface roughness or local structures of the electrodes. Light emission (or plasmon emission) in tunnel junctions or tunnelling induced light emission has been found and well characterized in many types of tunnel junctions, such as metal-insulator-metal (MIM) junction, scanning tunnelling microscope (STM) junctions, and molecular tunnel junctions.[5-7] Using an inverted optical microscope, we have worked on these three types of tunnel junctions and investigated the propagation properties of tunnelling electron excited plasmons on the metal electrode surface and the molecular electronic modulation of the plasmon excitation process.[8-10]

Figure S8 shows the mechanism for light emission (or plasmon emission) from our SAM-based tunnel junctions where the self-assembled monolayers of SC_{10} molecules (with HOMO-LUMO gap of 8-9 eV) works as the tunnel barrier. With an applied bias V_{Bias}, electrons in the top EGaIn electrode tunnel through the SAM layer to the gold bottom electrode. Because of the inelastic tunnelling process, the tunnel electrons have the chance to excite plasmon on the surface of the gold electrode. With an inverted optical microscope, the out-coupled photon or light emission can be recorded through the semi-transparent (40 nm thick) bottom gold electrode.

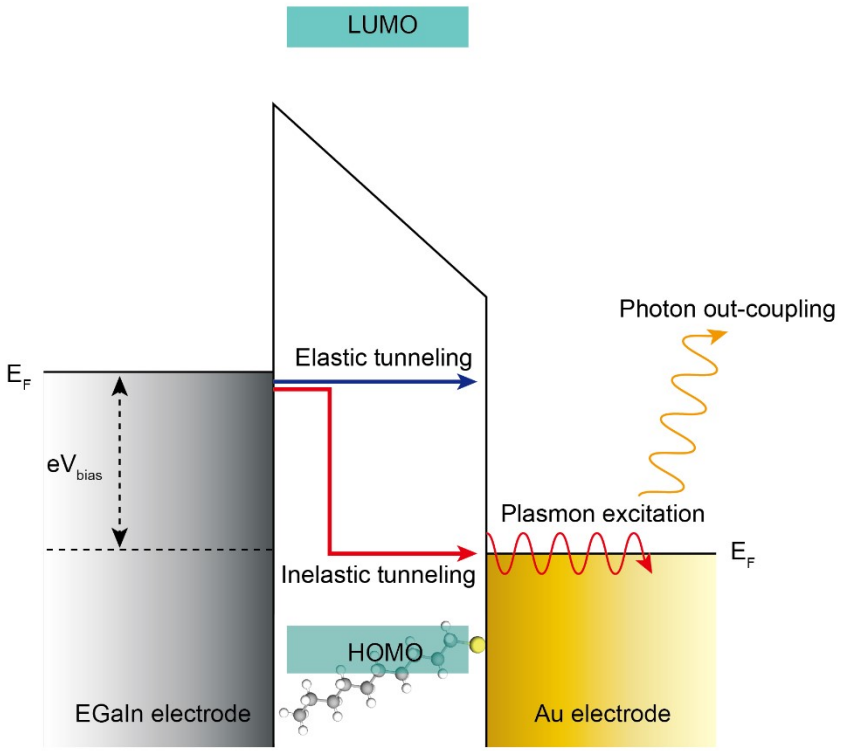

Figure S8. An energy level diagram of our SAM-based molecular tunnel junction with bias V_{Bias}. The red arrow indicates an inelastic tunnelling process for plasmon excitation.

S7. More examples of positive correlations.

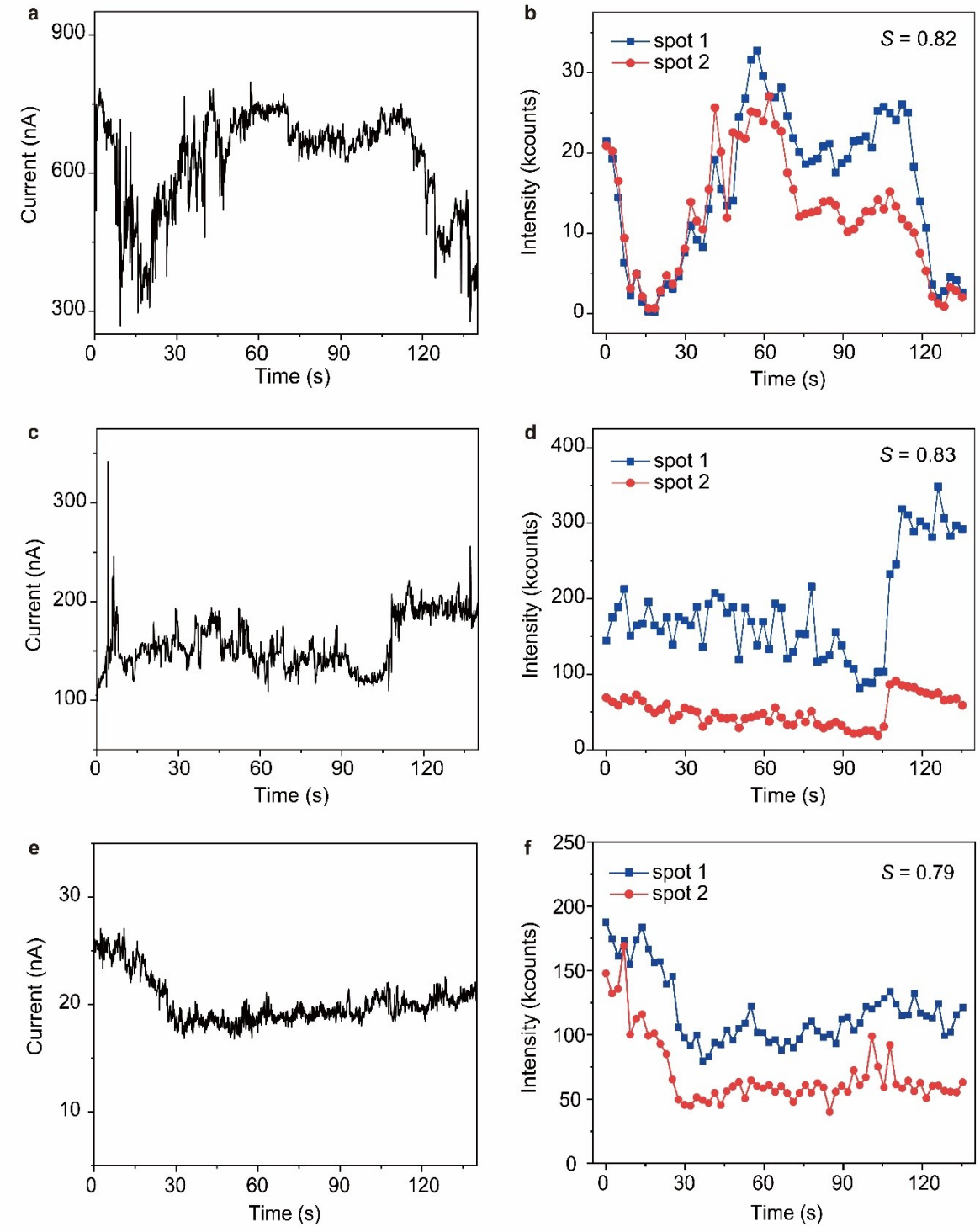

Figure S9. More examples of positive correlations. **a,c,e**) Time traces of electrical current for three different junctions. **b,d,f**) Time traces of the emission intensity for the two emitting spots in the three junctions.

S8. More examples of negative correlations.

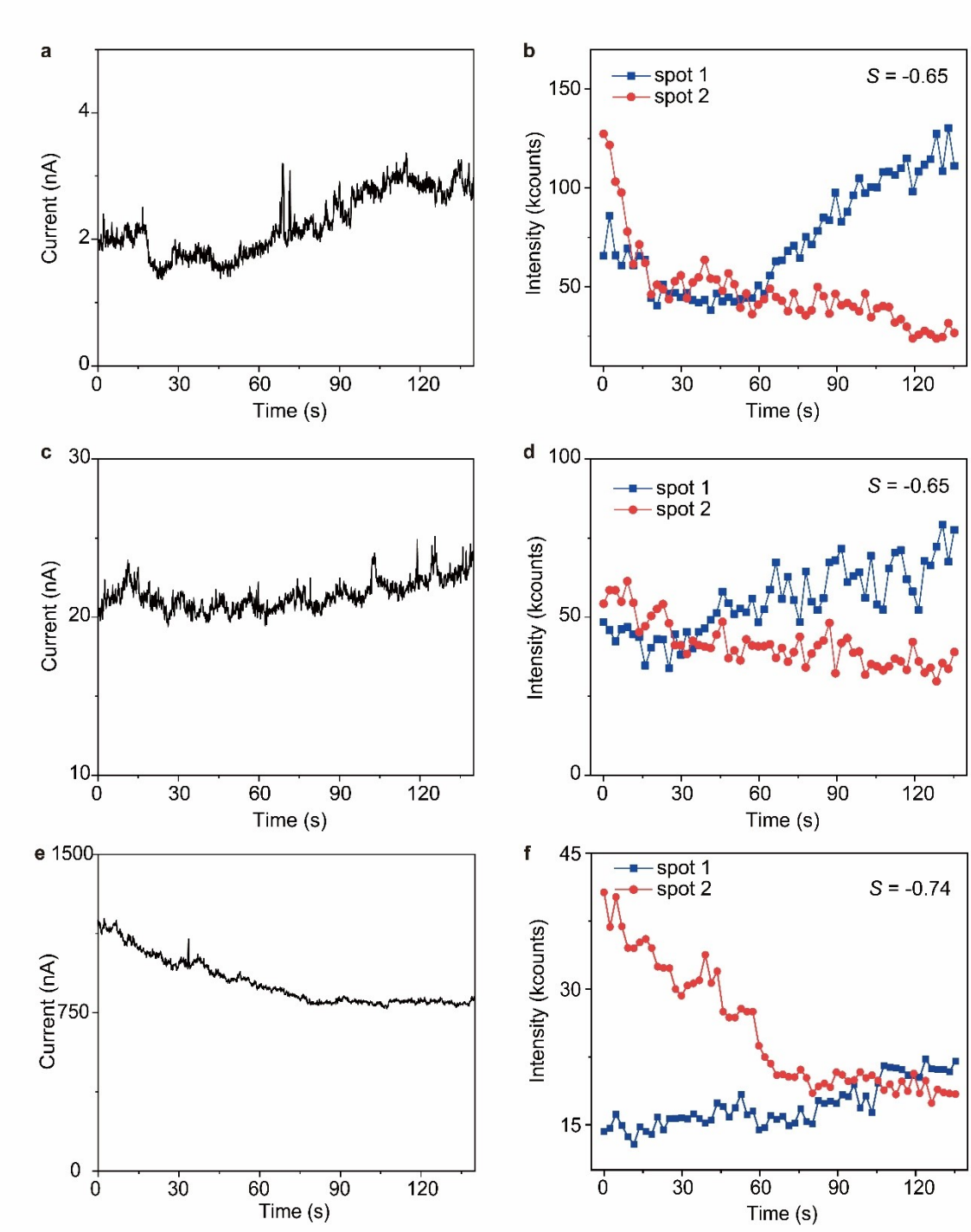

Figure S10. More examples of negative correlations. **a,c,e**) Time traces of electrical current for three different junctions. **b,d,f**) Time traces of the emission intensity for the two emitting spots in the three junctions.

S9. Degree of the correlation.

Table S1. One conventional rule for interpreting the degree of the correlation relation.[11]

Correlation coefficient *S*	Degree of the correlation
0.00 to 0.09 (or 0.00 to -0.09)	Negligible correlation
0.10 to 0.39 (or -0.10 to -0.39)	Weak positive (or negative) correlation
0.40 to 0.69 (or -0.40 to -0.69)	Moderate positive (or negative) correlation
0.70 to 0.89 (or -0.70 to -0.89)	Strong positive (or negative) correlation
0.90 to 1.00 (or -0.90 to -1.00)	Very strong positive (or negative) correlation

S10. Micropore junctions with varied numbers of emitting spots.

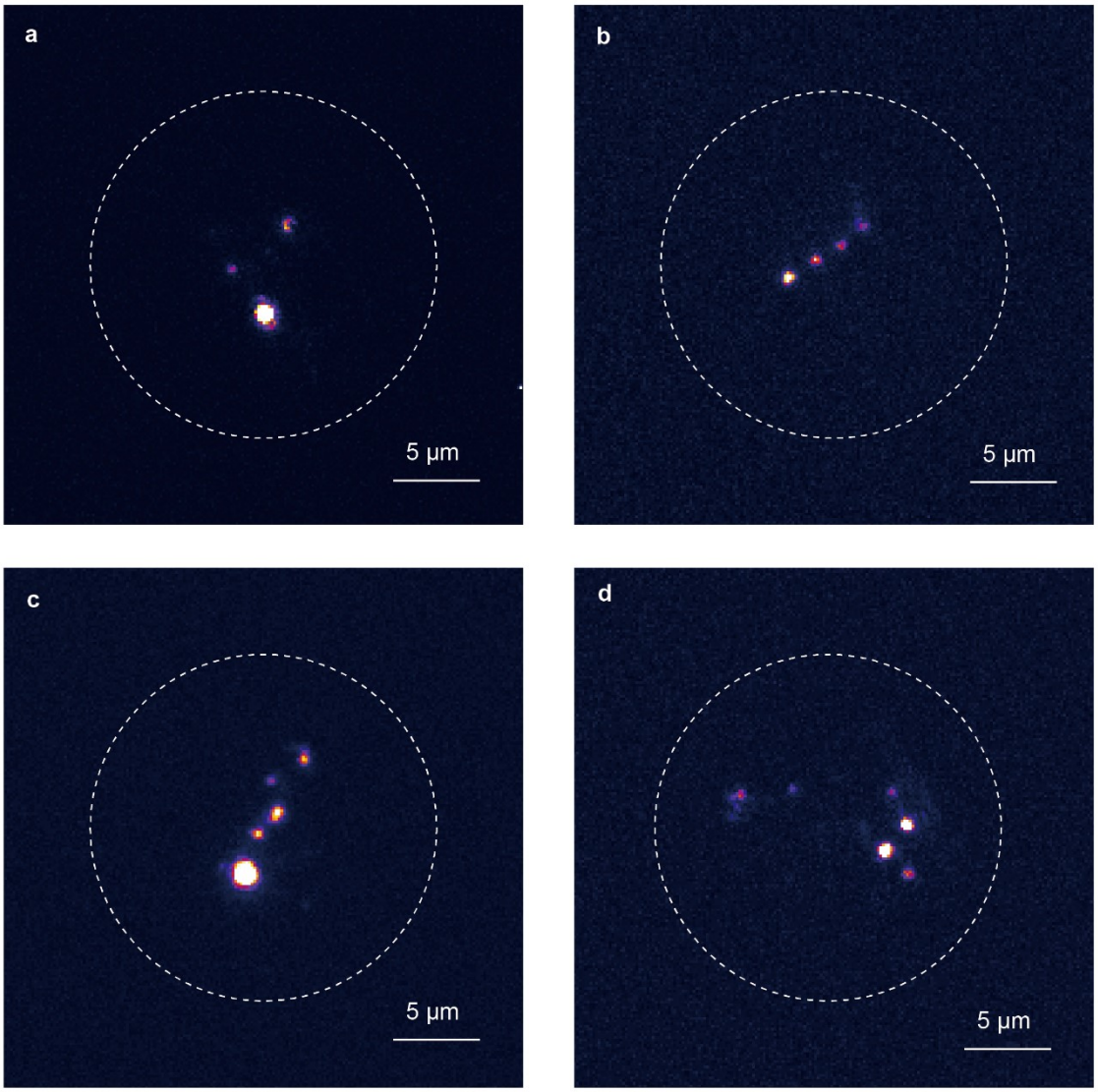

Figure S11. Optical images of the micropore junctions with varied numbers of emitting spots. **a**) Three emitting spots. **b**) Four emitting spots. **c**) Five emitting spots. **d**) Six emitting spots.

S11. Statistics of the correlation analysis.

Table S2. Statistics of the correlation analysis with varied numbers of emitting spots.

No. of emitting spots	No. of junctions
2	176
3	68
4	49
5	23
6	17

Table S3. Statistics of the correlation analysis under different bias.

Bias (V)	No. of junctions
1.6	29
1.7	58
1.8	74
1.9	74
2.0	58

S12. The quantitative deduction of the current change in the resistor model.

To better understand the current change in the resistor model shown in Figure 4a, we did the quantitative deduction. To simplify the calculation, the two parallel resistors are assumed to have the same resistance $R_{P1} = R_{P2} = R_0$. The series resistor represents the contact resistance R_{TC}. Here, it is worth mentioning that at a specific moment in the time trace, the electrical condition of the junction is fixed, i.e., the resistance of the contact resistor, the resistance of the conducting channel 1 and the resistance of the conducting channel 2 are all fixed. In this case, the resistance ratio between the contact resistor and the conducting channel resistor is also fixed, and we used a number α to name this ratio. Thus, in this initial state, with an applied bias V on the junction, the current through the two parallel resistors is the same and both can be written as:

$$I_1 = I_2 = \frac{1}{1+2\alpha}\frac{V}{R_0} \tag{S1}$$

As the bias applies, both the parallel resistance R_0 and the contact resistance R_{TC} may change for the next moment. On one hand, if one of the parallel resistance changes with a ratio of β, the current through the two parallel resistors will change to:

$$\begin{aligned} I_1' &= \frac{(1+\beta)}{(1+\beta)+\alpha(2+\beta)}\frac{V}{R_0} \\ I_2' &= \frac{1}{(1+\beta)+\alpha(2+\beta)}\frac{V}{R_0} \end{aligned} \tag{S2}$$

Thus, the current change ratio is:

$$\begin{aligned} \frac{I_1'}{I_1} &= \frac{(1+\beta)\,(1+2\alpha)}{(1+\beta)+\alpha(2+\beta)} \\ \frac{I_2'}{I_2} &= \frac{1+2\alpha}{(1+\beta)+\alpha(2+\beta)} \end{aligned} \tag{S3}$$

According to Eq. S3, Figure 4b shows the current change ratio as a function of the parallel resistance change ratio β, with the α value of 0.1.

On the other hand, if the contact resistance changes with a ratio of γ, the current through the two parallel resistors will change to:

$$I_1'' = I_2'' = \frac{1}{(1+2\alpha+2\alpha\gamma)}\frac{V}{R_0} \tag{S4}$$

Thus, the current change ratio is:

$$\frac{I_1''}{I_1} = \frac{I_2''}{I_2} = \frac{(1+2\alpha)}{(1+2\alpha+2\alpha\gamma)} \tag{S5}$$

According to Eq. S5, Figure 4c shows the current change ratio as a function of the contact resistance change ratio γ, with the α value of 0.1.

In the main text, we show the current change ratio as a function of the parallel resistance change ratio β or the contact resistance change ratio γ with the α value of 0.1. Figure S12 further shows the current change ratio as a function of β or γ with the α value of 0.2 (Figure S12 a-b), 0.3 (Figure S12 c-d). and 0.4 (Figure S12 e-f), respectively. Figure S12 indicates that although the current change ratio varies, the α value does not influence the correlation relation type (positive or negative) between the current through the two conducting channels.

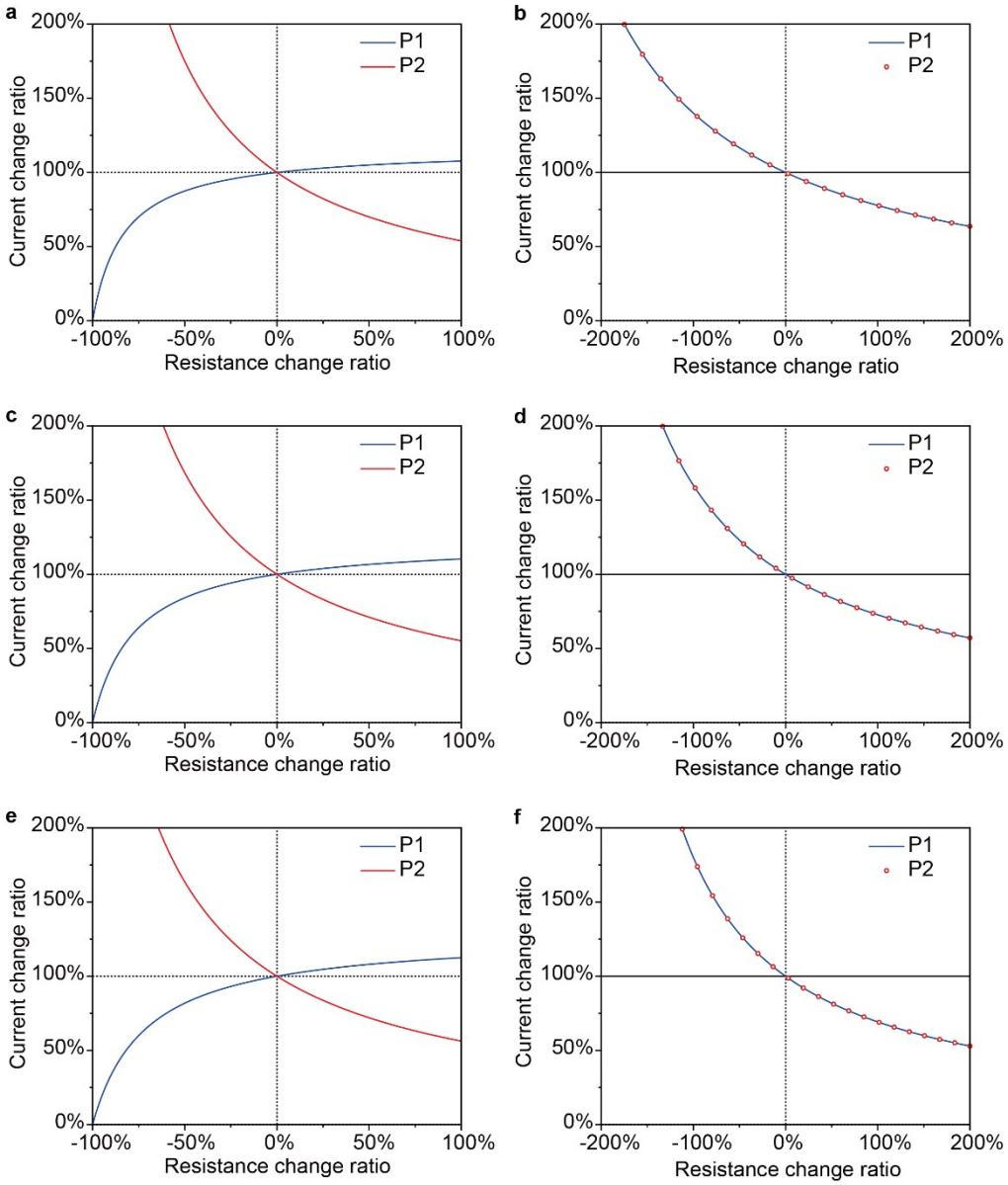

Figure S12. a) Current change ratio of the two conducting channels as a function of the resistance change ratio β with the α value of 0.2, showing negative correlation between the two conducting channels. **b**) Current change ratio of the two conducting channels as a function of the resistance change ratio γ with the α value of 0.2, showing positive correlation between the two conducting channels. **c**) The same as a) but with α value of 0.3. **d**) The same as b) but with α value of 0.3. **e**) The same as a) but with α value of 0.4. **d**) The same as b) but with α value of 0.4.

S13. The average effect of conformation change in the conducting channels.

It is worth to note that the channel resistances R_{P1} and R_{P2} should represent the statistical average of the electrical characteristics from multiple molecules in each conducting channel. In our measurements, the light emission intensity changes are mostly less than 3 times (e.g. Figure 2 and Figure S10), which indicates R_{P1} and R_{P2} fluctuation or current fluctuation in the conducting channel at the same level. This fluctuation level is actually quite small.

We could estimate the current fluctuation induced by the molecular conformation change as follows.[12] Without conformation change, the current density J can be described by the general tunnelling equation (Equation S6)

$$J = J_0 e^{-\beta_1 d_0} \tag{S6}$$

With conformation change of Δd in length, the tunnel barrier can be described as a double barrier junction by Equation S7 with a gap of air

$$J' = J_0 e^{-\beta_1 (d_0 - \Delta d)} e^{-\beta_2 \Delta d} \tag{S7}$$

where β_1 and β_2 are the tunnelling decay coefficient of the alkane-thiolate and air, respectively; d_0 is the molecular length, J_0 is the hypothetical current density. Thus, the current density change J'/J is written as:

$$\frac{J}{J'} = \frac{J_0 e^{-\beta_1 d_0}}{J_0 e^{-\beta_1 (d_0 - \Delta d)} e^{-\beta_2 \Delta d}} = \frac{e^{\beta_2 \Delta d}}{e^{\beta_1 \Delta d}} \tag{S8}$$

With the value of β_1 = 0.8 Å^{-1} for aliphatic SAMs and the value of β_2 = 2.9 Å^{-1} for air,[5,12] a value of Δd = 1.2 Å (the length of just one CH_2 group) will induce a current density change (J'/J) about 12.4 times. Moreover, for a current fluctuation of 3 times, the conformation change is only to be about 0.53 Å. Such a conformation change shall be quite easy to realize by bending and rotation around the multiple C-C bonds of the molecules such as decanethiols.

By considering the molecular number in each conducting channel (see Supplementary Section S5), the possible fluctuation in each conducting channel will be due to an average conformation change (e.g. some molecules in the conducting channel stays unchanged, some molecules change their conformation) of multiple molecules.

S14. Correlation relation with the BPT SAMs.

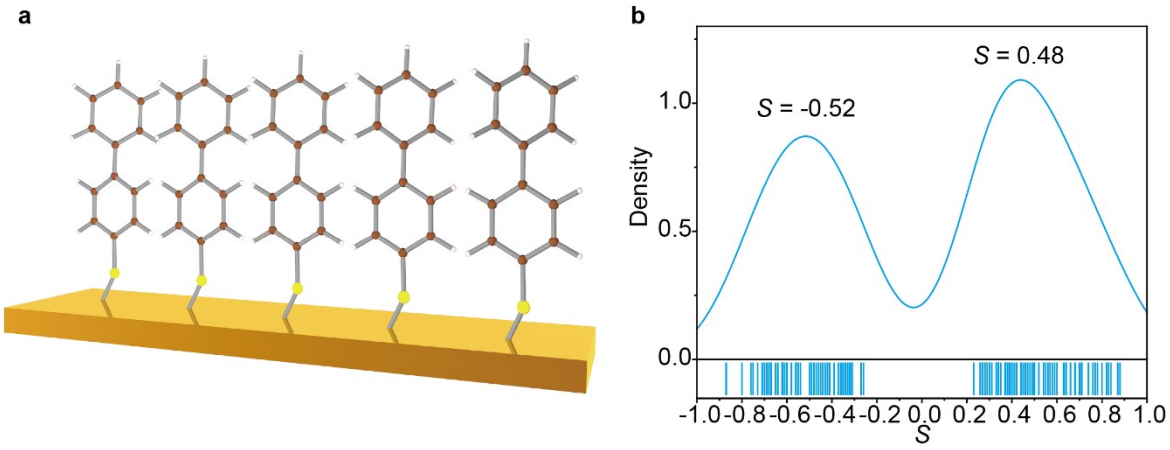

Figure S13. a) Schematic illustration and **b**) *S* distribution of BPT SAMs on Au^{TS} bottom electrode.

S15. Correlation relation with the Ag^{TS} bottom electrode.

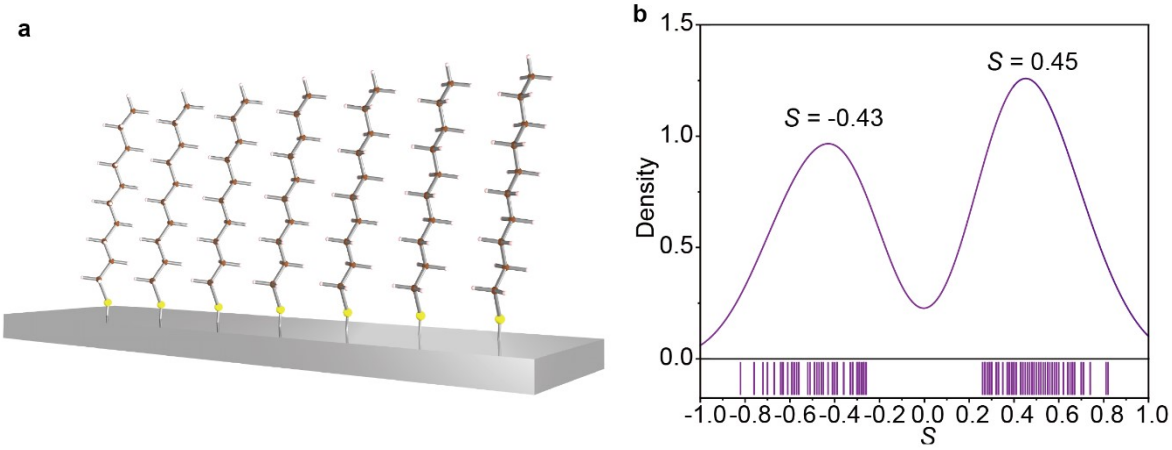

Figure S14. a) Schematic illustration and **b**) *S* distribution of SC_{10} SAMs on Ag^{TS} bottom electrode.

References

1. L. Yuan, L. Jiang, B. Zhang, C. A. Nijhuis, *Angew. Chem. Int. Ed.*, 2014, **53**, 3377–3381.
2. A. Wan, L. Jiang, C. S. S. Sangeeth, C. A. Nijhuis, *Adv. Funct. Mater.*, 2014, **24**, 4442–4456.
3. W. Du, T. Wang, H. S. Chu, L. Wu, R. Liu, S. Sun, W. K. Phua, L. Wang, N. Tomczak, C. A. Nijhuis, *Nat. Photon.*, 2016, **10**, 274–280.
4. B. Xu, N. J. Tao, *Science*, 2003, **301**, 1221–1223.
5. T. Wang, C. A. Nijhuis, *Appl. Mater. Today.*, 2016, **3**, 73–86.
6. R. Gutzler, M. Garg, C. R. Ast, K. Kuhnke, K. Kern, *Nat. Rev. Phys.*, 2021, **3**, 441–453.
7. M. Wang, T. Wang, O. S. Ojambati, T. J. Duffin, K. Kang, T. Lee, E. Scheer, D. Xiang, C. A. Nijhuis, *Nat. Rev. Chem.*, 2022, **6**, 681–704.
8. Y. Zhu, L. Cui, M. Abbasi, D. Natelson, *Nano Lett.*, 2022, **22**, 8068–8075.
9. T. Wang, E. Boer-Duchemin, Y. Zhang, G. Comtet, G. Dujardin, *Nanotechnol.*, 2011, **22**, 175201.
10. W. Du, T. Wang, H. S. Chu, C. A. Nijhuis, *Nat. Photon.*, 2017, **11**, 623–627.
11. P. Schober, C. Boer, L. Schwarte, *Anesth. Analg.*, 2018, **126**, 1763–1768.
12. T. Wang, W. Du, N. Tomczak, L. Wang, C. A. Nijhuis, *Adv. Sci.*, 2019, **6**, 1900390.